Materials and Design 107 (2016) 511–519

Contents lists available at ScienceDirect

Materials and Design

journal homepage: www.elsevier.com/locate/matdes

Martensitic transformation strain and stability of Ni_{50-x}–Ti_{50}–Co_x ($x = 3, 4$) strips obtained by twin-roll casting and standard processing techniques

L. Isola [a], P. La Roca [b,c], C. Sobrero [a], V. Fuster [a], Ph. Vermaut [d,e], J. Malarría [a]

[a] Instituto de Física Rosario (CONICET-Universidad Nacional de Rosario) Bvrd, 27 de Febrero 210 Bis, S2000EZP Rosario, Argentina
[b] Centro Atómico Bariloche, Comisión Nacional de Energía Atómica (CNEA), Av. Ezequiel Bustillo 9500, 8400 S. C. de Bariloche, Argentina
[c] Instituto Balseiro (UNCuyo), Av. Ezequiel Bustillo 9500, 8400 S. C. de Bariloche, Argentina
[d] Chimie ParisTech, PSL Research University, CNRS, Institut de Recherche de Chimie Paris (IRCP), F-75005 Paris, France
[e] Sorbonne Universities, UPMC University Paris 06, UFR926, 75005 Paris, France

ARTICLE INFO

Article history:
Received 22 March 2016
Received in revised form 20 May 2016
Accepted 11 June 2016
Available online 18 June 2016

Keywords:
NiTi alloys
Shape memory
Twin-roll casting
Mechanical properties
Texture

ABSTRACT

The martensitic transformation properties (maximum strain, residual strain and transformation stability) of Ni_{50-x}–Ti_{50}–Co_x strips produced by twin-roll casting (TRC) and standard casting (SC) were compared. A complete microstructural characterization was carried out on both samples using optical microscopy, transmission electron microscopy (TEM), electron backscattering diffraction (EBSD-SEM), energy dispersive X-ray spectroscopy (EDS-SEM), X-Ray diffraction and differential scanning calorimetry (DSC). According to the results obtained by DSC and load-biased thermal-cycling measurements, the TRC strip is more stable and has lower residual strain than the SC strip for loads below 90 MPa. Using the austenitic texture of each strip, the recoverable strain upper bounds of the martensitic transformation (Sachs' bound) were calculated. A comparison between the measured maximum recoverable strain and the Sachs' bound, allows us to discuss how the particular microstructures produced by the two production techniques affect the strip's shape memory properties.

1. Introduction

Ni–Ti shape memory alloys (SMA) are recognized for their remarkable functional and physical properties: large recoverable strains; corrosion resistance; and biocompatibility [1]. The addition of *Co* to *Ni–Ti* alloys produces a shift of $M_s^{(B19')}$ downwards into a lower temperature range [2–4], which is more appropriate for some dental applications [5], increases the yield strength [6], and improves the stiffness [7]. Moreover, *Ni–Ti–Co* has biocompatibility properties similar to the binary alloy [8] and the addition of Co enhances greatly the corrosion resistance in an artificial urine solution [9].

In the recent past, different advanced techniques have been used to tune or tailor the microstructure and shape in order to improve mechanical and functional properties of SMA [10–13]. Among these, twin-roll casting (TRC), a rapid solidification technique, has been introduced to obtain sheets with small grain size in a single processing step [14–16]. TRC has several advantages over traditional methodologies. It is a method, where the total cost and time is reduced, by avoiding the lengthy thermomechanical treatment needed for conventional casting and metallurgical processes. Rapid solidification procedures also lead to a product with a microstructure of unusual and interesting features: these strip microstructures are characterized by strongly textured $[001]_{B2}$ columnar grains parallel to the normal direction (ND), and a mixture ranging from $[100]_{B2}$ to $[110]_{B2}$ directions in the rolling (RD) and transverse directions (TD) [17] (directions of type $[uv0]_{B2}$, distributed between $[100]_{B2}$ and $[110]_{B2}$, lie parallel to the strip plane).

Many practical applications of shape memory alloys require a large number of thermomechanical cycles and a stable shape memory effect [18]. Therefore, SMA properties are usefully characterized by the transformation temperatures and the recoverable and residual strain during thermal cycling. Another important parameter is the transformation hysteresis, e.g. a small hysteresis is required for fast actuation applications (such as MEMSs and robotics) [1].

In a polycrystalline SMA, the austenitic texture sets an upper bound to the maximum recoverable strain [19,20]. This upper bound, called the Sachs' bound, is assessed assuming that the most favorable and unique martensite variant grows in each grain in order to induce maximum deformation [21,22]. Nevertheless, the real recoverable strain could be lower than the Sachs' bound [23] and might change with the successive cycles [24,25].

E-mail address: malarria@ifir-conicet.gov.ar (J. Malarría).

http://dx.doi.org/10.1016/j.matdes.2016.06.049
0264-1275/

The residual strain during thermo-mechanical cycling results from a number of factors, the most important being plasticity, caused by lattice mismatch between austenite and martensite [26] and martensite pinning by defects [27].

The goal of this work is to compare the properties (maximum strain, residual strain and transformation stability) of the Ni_{50-x}–Ti_{50}–Co_x ($x = 3, 4$) strips produced by two different techniques (standard processing and twin-roll casting) and to perform a detailed analysis of the results taking into account the microstructural characteristics of the two kinds of strips.

2. Experimental set-up

The twin-roll casting technique consists of the solidification of a melted alloy between two symmetrical rollers, which produces a continuous solid sheet. These rollers rotate at high speed in opposite directions. The entire system is located in a chamber with a helium atmosphere in order to prevent oxidation and improve thermal stability. The melted alloy, placed in a quartz nozzle, is injected into the roll gap by argon gas pressure. The processing parameters for the Ni_{47}–Ti_{50}–Co_3 strip are given in Table 1. A more detailed description can be found in reference [28].

In order to produce strips by a standard processing technique (this technique will be referred with acronym of Standard Casting *SC*), Ni_{46}–Ti_{50}–Co_4 alloy ingots were produced in a high-frequency induction furnace under an argon atmosphere. The ingots were 50 mm long and 10 mm in diameter. These ingots were hot rolled at 1073 *K* to reduce the thickness to 3.5 mm. Then, the sheets were room temperature rolled to 0.5 mm in several steps with intermediate anneals at 1073 *K*. The final thickness reduction, after the last intermediate anneal, was 39%. Finally, the strips were annealed at 873 *K* for 10 minutes followed by water quenching.

The transformations were characterized with a Mettler differential scanning calorimeter (DSC). The DSC measurements for each cycle started by cooling the strips from 340 K to 140 K at a rate of 10 K/min. The samples were held at 140 K for 5 min and then reheated to 340 K at a rate of 10 K/min. At 340 K, the samples were held for 5 min. The characteristic direct and reverse transformation temperatures were determined as the intersection between the interpolated baseline and the tangents to both sides of the peak.

Strip microstructures were observed using an Olympus PME3 optical microscope, an FEI-FEG Quanta 200 scanning electron microscope (SEM) using a TSL-EDAX EBSD system, a Leitz AMR 1000 SEM using an Oxford Silicon Drift Detector for EDS analysis and an FEI TECNAI F20 transmission electron microscope (TEM). The specimens were mechanically polished through 1 μm diamond paste and etched with an aqueous solution of 10 vol.%*HF* p.a. and 40 vol.%HNO_3 p.a. for the optical analysis. The SEM samples were mechanically polished and finished with colloidal silica to give an average surface roughness appropriate for EBSD experiments. The thin foils examined in the TEM were prepared with double-jet polishing using 95 vol.% Acetic Acid (CH_3COOH) and 5 vol.% Perchloric Acid ($HClO_4$).

The diffraction patterns and pole figures were taken with a Philips X′ Pert Pro MPD diffractometer, using Cu $\alpha_1\alpha_2$ lines at 40 kV and 30 mA. The diffractometer was equipped with an X-ray lens optics, parallel plaques and a graphite monochromator moderating the outgoing beam and an Eulerean Cradle for texture measurements. A heating stage [29] was used to measure the pole figure of the SC strips in the austenitic state (these samples are completely austenitic at 360 K). Measured pole figures were corrected for defocussing and background and further analyzed by WXpopLA [30] to obtain orientation distribution functions and guarantee pole figure compatibility.

The diffractograms were collected moving from 25° to 85°, in 0.02° angular 2θ steps, with a collecting time per step ranging from 2 s for regular scans to 10 s for refinement purposes. Rietveld refinement of X-ray diffraction patterns was done using Maud version 2.55 [31]. This program allows us to incorporate microstructural and texture analysis into the traditional refinement. The standard chosen to account for instrument artifacts was LaB_6 [32].

Load-biased thermal cycling was performed in a custom-built machine, that allowed us to apply a constant load and program cooling/heating cycles. The machine has an Instron load cell (1 k*N*) to measure the stress. The strain is measured by an *Epsilon* 3542 axial extensometer with a 10 mm gauge length, clipped between the specimen grips. The sample and grips were enclosed in a cylindrical acrylic chamber and cooled with nitrogen vapor. Two tubular electric cartridge heaters were inserted into holes drilled into the grip body for sample heating. A more detailed description can be found in reference [22]. The rectangular dog-bone shape tension specimens used in the load-biased thermal cycling experiments had gauge dimensions of $(13 \times 4.5 \times 0.35)$ mm^3 (TRC) and $(13 \times 4.5 \times 0.45)$ mm^3 (SC). They were cut from the strips in a spark-cutting machine.

Table 1
Twin-roll casting parameters.

Material	$Ni_{47}Ti_{50}Co_3$
Melt temperature (*K*)	1783
Roller material	*CuCoBe*
Rollers speed (ms^{-1})	0.6
Ejection pressure (mbar)	250

3. Results

3.1. Microstructural characterization

Clearly observed in Fig. 1(a), the microstructure of the TRC strip has transversely elongated grains growing from both surfaces up to an interface located in the strip core. This feature is characteristic of the rapid-solidification process. Fig. 1 (b) shows an SEM-EBSD normal-direction grain map of the TRC strip surface. A rather uniform equiaxial structure of strongly textured grains can be seen in this image (which will be further discussed in Subsection 3.4). The grains sizes are of the order of 6 μm–20 μm in this section and 100 μm in the elongated direction.

On a finer scale, TEM observations normal to the strip surface show a typical cellular solidification structure. The grains observed in EBSD image (Fig. 1 (b)) are composed of cells with a characteristic dimension of 1 μm (Fig. 2 (a)), which are delineated by precipitates. The precipitates were identified as Ti_4Ni_2O (Fig. 2 (b)), as it will be further discussed in Subsection 3.2. Only a few randomly distributed dislocations were observed in TEM images.

In marked difference to the TRC material, the SC sample microstructure contains features typical of rolling. Figs. 3 and 4, optical and TEM bright-field images respectively, show the SC microstructure after a final reduction of 39% followed by annealing at 873 K and quenching. The average grain size of the SC strip is about 20 μm. These grains are highly deformed, which is evidenced by the elevated number of dislocations observed in the TEM image (Fig. 4). In addition, the grains are subdivided into small cells or subgrains of less than 1 μm diameter.

No precipitates could be detected in X-Ray diffraction patterns taken at 360 K, only austenite reflections are visible (Fig. 5 (a)).

3.2. Phase characterization

Due to small variations in each strip's production process or the precipitation of other phases, the austenite composition may differ from the nominal. As the martensitic transformation is very sensitive to the

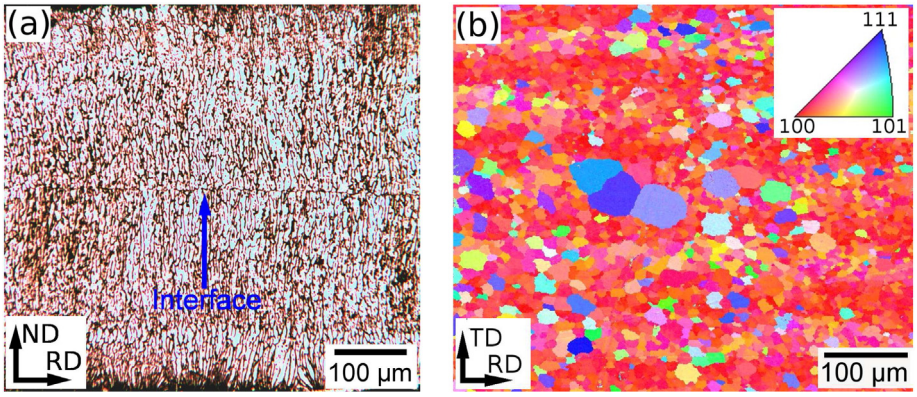

Fig. 1. TRC strip: Optical micrograph of the transverse section (the blue arrow indicates the interface between the two solidification fronts) (a), and a SEM-EBSD normal direction grain map of the surface (the inverse pole figure in the inset shows the reference color map) (b).

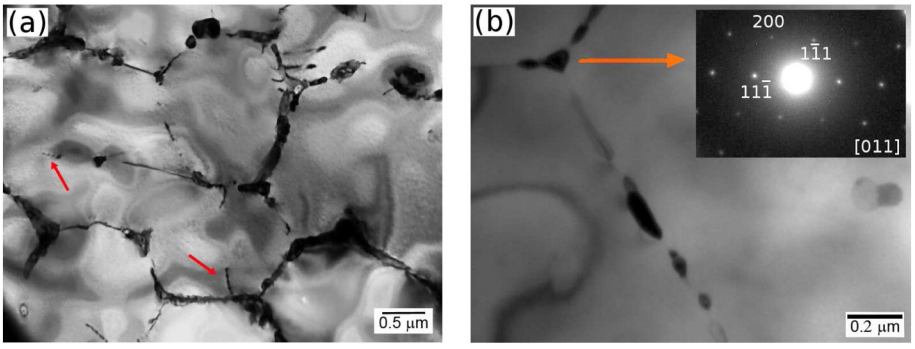

Fig. 2. Typical TEM bright field images of TRC strip: a grain divided into cells (delineated by precipitates), where few dislocations can be seen (indicated by arrows)(a) and Ti_4Ni_2O precipitates in cell boundary (b).

chemical composition, these variations could produce modifications in the transformation temperatures.

The strip chemical compositions were measured by quantitative EDS-SEM using pure *Ni*, *Ti* and *Co* samples as reference materials. In order to measure the strip's average composition, the EDS spectra were collected with a scanning electron probe using a window of about 540 μm–440 μm. The results, shown in Table 2, are close to the nominal compositions.

The diffractograms from both samples are shown in Fig. 5 (a) and (b). The SC strip was entirely austenitic, as observed in Fig. 5 (a). The main characteristic peaks of all the phases are labeled according to the corresponding Miller indexes.

With respect to the TRC specimen, two phases were identified: austenite as the major component and an oxide in the form of precipitates.

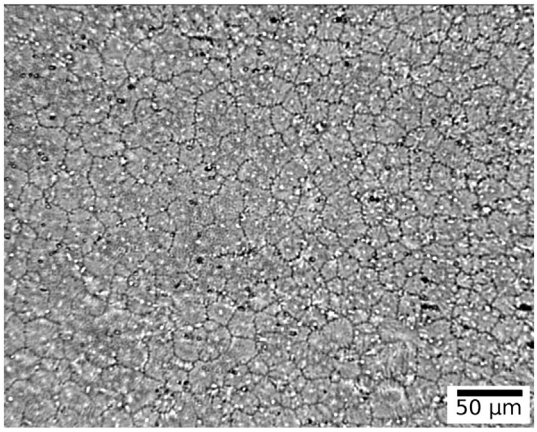

Fig. 3. Optical micrograph of the SC strip.

Our refinement results showed that TRC produced a high purity strip, containing more than 98 ± 1 wt.% austenite. Its structure was cubic of the B2-type having the Pearson symbol *cP*2, which corresponds to the space group $Pm\bar{3}m$ (N° 221 [33]). The lattice parameter determined from the refinement is 0.3020 nm, which is very similar to the $Ni_{50.7}Ti_{49.3}$ cell value [34]. This confirms the slight influence of Co chemical substitution on the crystal structure of the parent phase. On the other hand, the precipitates observed in the TRC strip were identified as Ti_4Ni_2O (see Fig. 5 (b)). This oxide has a cubic A4-type structure with the Pearson symbol *cF*8, with the space group $Fd\bar{3}m$ (N° 227 [33]), and it has a refined cell parameter equal to 1.1306 nm. The refined amount of oxide was 2 ± 1 wt.%, which means the oxygen content is around 0.3 at.% in the TRC strip. The quality of the refinement can be appreciated in Fig. 5.

The strong texture is readily seen in Fig. 5 (b), especially considering the low intensity measured for the austenitic main reflection at $2\theta = 42.39°$, which results from the {110} planes in diffraction condition. Moreover, the intensity of the {200} plane reflections is substantially increased when compared to the same material with a random distribution of crystallites. In this work, the intensity correction of the X-ray spectra to account for texture was done using the arbitrary texture model implemented in Maud.

3.3. Transformation temperatures

The DSC curves of both materials are shown in Fig. 6. Two subsequent martensitic transformations take place on cooling in both samples. The first DSC exothermic peak corresponds to the transformation of the *B*2 parent phase to the rhombohedral *R*-phase, while the second exothermic peak is associated with the *R*-phase to the monoclinic *B*19′ phase transformation. The phases present before and after each thermal

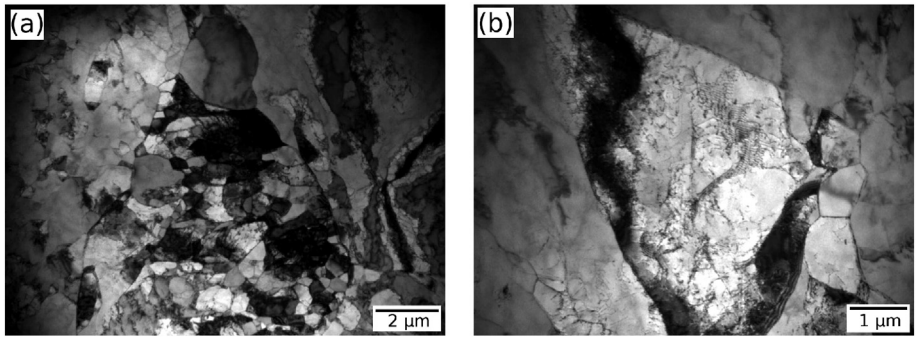

Fig. 4. TEM bright field images of the SC sample. The grains are subdivided into cells (a) and many dislocations can be observed inside the grains (b).

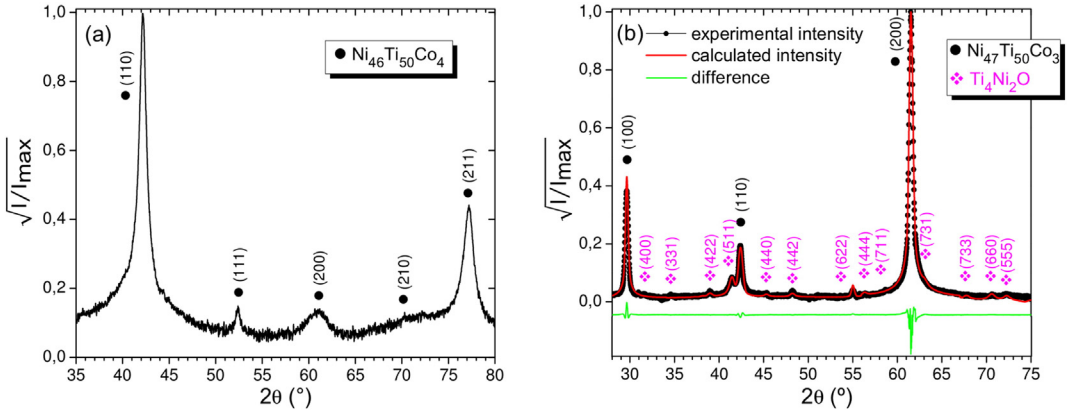

Fig. 5. X-ray difraction patterns of the SC (a) and TRC strips (b) measured at 360 K and room temperature, respectively. In figure (b), it is also displayed the refined curve and difference between the experimental pattern and the calculated profile using Maud. The square root of the normalized intensity is plotted against the 2 θ angle, to show low-intensity diffraction peaks.

event have been already studied [35,36]. Note that the transformation to *R*-phase is promoted by addition of *Co* and the consequent shift of $M_S^{(B19')}$ downwards over a lower temperature range. The second peak of the TRC strip is extended over a wider temperature range than that of the SC strip. This is probably due to small differences in the local composition of the austenite phase produced by Ti_4Ni_2O precipitation [37,38]. On the other hand, during heating two overlapping endothermic peaks were observed in the case of the TRC strip (the higher peak corresponds to the *B*19′ to *R*-phase transformation followed by the *R*-phase to parent phase transformation peak [36]). The SC strip displays only a single endothermic peak in the first cycles, which begins to split into two peaks after 50 cycles. These two peaks are clearly observed in the 100 cycle.

It is worth mentioning that DSC curves of the TRC strip show only a slight decrease of transformation temperature with thermal cycling, i.e. higher thermal stability is found. To the contrary, the DSC curves of the SC strip noticeably change with cycling. That is, the M_s value of the SC strip decrease rapidly with the first thermal cycles, about 30 K in the first 11 cycles. After 12 cycles, a smoother decrease is observed in the M_s value, of around 0.1 K per cycle. The marked transformation temperature decrease observed in the SC sample with thermal cycling may be associated with an important degree of microplasticity activity (introduction of dislocations) induced when the material is cycled through the martensite transformation. In this kind of specimen, many tangled dislocations are introduced in the rolling procedure. Such dislocations are not fully removed in the final thermal treatment, performed at 873 K, in order to preserve some degree of stiffness in the matrix. So, when the austenitic transformation is induced, moving interfaces must overcome obstacles, dislocation tangles, already present in the matrix at the beginning of the cycling procedure. As a consequence, new dislocations are introduced and in a subsequent cycle additional cooling is necessary to achieve the martensitic transformations [18,39,40]. This phenomenon is clearly observed in the first stage of cycling (cycle 1 to 11 in our case), and then it remains present, although drastically (or significantly) reduced, in the subsequent cycles.

Table 2
Strip compositions measured by EDS-SEM.

Element	TRC (at.%)	SC (at.%)
Ti	50.3 ± 0.5	50.4 ± 0.5
Ni	46.7 ± 0.5	45.6 ± 0.5
Co	3.0 ± 0.5	4.0 ± 0.5

The transformation temperatures and heats of transformation after reaching the quasi-stable condition are listed in Table 3 (the 5 and 11 cycles of the TRC and SC samples, respectively). Note that the transition temperatures of the TRC strip are at least 40 *K* lower than those of the SC strip. This may be surprising since the addition of *Co* yields a decrease of the transformation temperatures and the *Co* content of the SC strip is 1 at.% higher than that of the TRC strip [2]. Nevertheless, the Ti_4Ni_2O precipitation produces *Ni*-enrichment of the matrix, and it yields a decrease of the TRC transformation temperatures. Using a similar calculation from reference [37] and the precipitate concentration determined by the Rietveld refinement (2 ± 1 wt.% in the TRC strip), the Ni concentration is 47.3 ± 0.2 at.% in the matrix (instead of the expected 47 at.%). This very low *Ni*-enrichment of the matrix could explain the transformation temperature decrease. The particular properties of the process, highly out of equilibrium, would be another factor shifting the transformation temperatures to lower values [28]. The heats of transformation values are in good agreement with the values reported in literature [28,41–43]. It is necessary to point out that the heat of transformation values for the TRC strip are lower than those measured in the SC strip. Similar results were obtained in the *Ni–Ti* binary alloy [28].

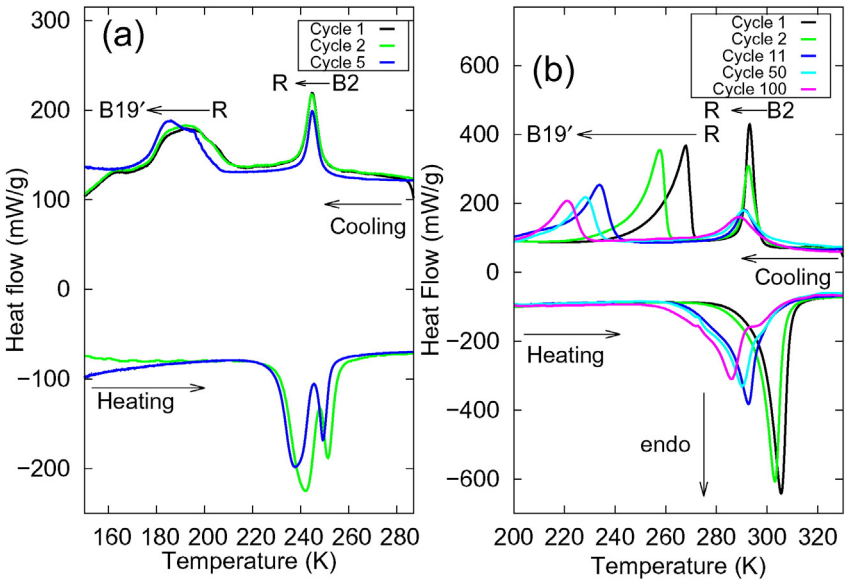

Fig. 6. DSC curves. (a) TRC (b) SC strips.

3.4. Texture

Pole figures are shown in Fig. 7. The austenite pole figures of the TRC sample were measured at room temperature, while those of the SC sample were measured at 360 *K* in order to ensure that the sample was completely austenitic (see Fig. 6 (b)).

The strong texture in the $\{100\}_{B2}$ pole figure is typical of the TRC strip. Its maximum normalized intensity is about 40 times random in the normal direction (ND) to the strip surface. The $\{110\}_{B2}$ pole figure has a maximum at $\theta = 45$, and an almost random distribution in azimuthal angle with a small local maximum in the rolling (RD) and transverse direction (TD). This means that the *B2* cubic structure has a face parallel to the strip surface (this can be observed in many grains in Fig. 1(b)) and an almost random distribution of directions in the strip plane.

The pole figures of the SC strip show a γ-fiber texture. This texture is characterized by a $\{111\}_{B2}$ pole parallel to the *ND*. This is clear in the *ND* inverse pole figure, Fig. 8(b). Therefore, the directions at and close to the $\langle 110\rangle_{B2}$ direction are the main components in the *RD* inverse pole figure. These results are consistent with those reported by Laplanche et al. [44] for NiTi alloys after cold rolling and subsequent recrystallization.

3.5. Sachs bound calculation: $B2 \rightarrow B19'$ transformation strain

The upper bound or Sachs bound of the recoverable transformation strain is calculated assuming that the most favorable and unique martensite variant grows in each of the grains, inducing maximum deformation [45,22]. So in each of the grains, the transformation strain can be calculated from the lattice distortion due to the $B2 \rightarrow B19'$ martensite transformation. Fig. 9 shows the simulated maximum transformation strain (ε_M) for each direction expressed by contour lines in the stereographic triangle. In the ε_M assessment, the lattice constants for $Ni_{50.7}Ti_{49.3}$ (235 *K*) [34] are used: $a_0 = 0.30069(4)$ nm for the *B2* phase and $a = 0.28786(2)$ nm, $b = 0.41340(2)$ nm, $c = 0.46215(4)$ nm and $\beta = 96.474(8)°$ for the $B19'$ phase.

Then, the Sachs bound is calculated averaging ε_M on the inverse pole intensities (I^i). This can be done with the following expression [21]:

$$\overline{\varepsilon}_M = \frac{\sum_{i=1}^{N} \varepsilon_M^i I^i}{\sum_{i=1}^{N} I^i} \tag{1}$$

where $N = 361$, which is the number of points in the inverse pole figure accounting for the polycrystal texture. Using the rolling-direction inverse pole figures shown in Fig. 8, the Sachs bounds in the rolling direction are (5.6 ± 0.5) % for the TRC strip and (8.9 ± 0.7) % for the SC strip. The uncertainties were estimated measuring the texture in different parts of the strips and taking into account the lattice distortion produced by *Co* additions [22]. These Sachs bound values suggest, a priori,

Table 3
Transformation temperatures and heats of transformation after reaching the quasi-stable condition (the 5 and 11 cycles of the TRC and SC samples, respectively). R_s^c: *R*-phase start during cooling, M_s: $B19'$ martensite start, M_f: $B19'$ martensite finish, R_s^h: *R*-phase start during heating, A_s: austenite start and A_f: austenite finish and *Q*: heat of transformation.

Sample	R_s^c (K)	$Q^{B2\rightarrow R}$ (J/g)	M_s (K)	M_f (K)	$Q^{R\rightarrow B19'}$ (J/g)	R_s^h (K)	A_s (K)	A_f (K)	$Q^{B19'\rightarrow B2}$ (J/g)
TRC	249	−6.1	207	174	−14	230	245	253	21
SC	298	−9.5	240	218	−19	—	284	298	29

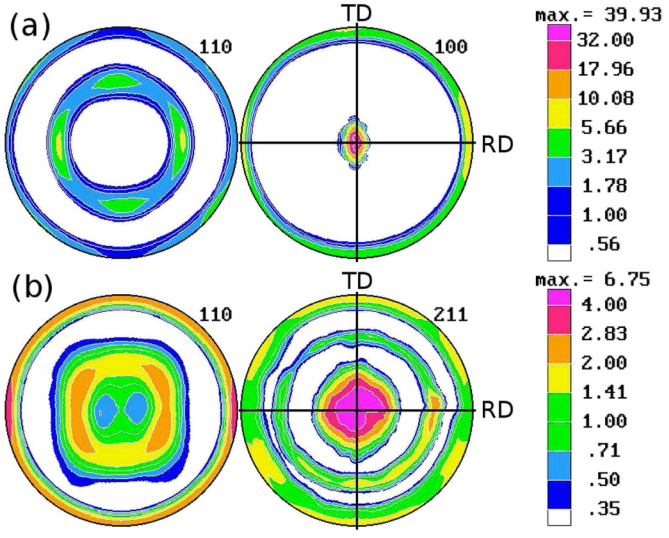

Fig. 7. Pole figures. (a) TRC sample measured at room temperature (b) SC sample measured at 360 *K*.

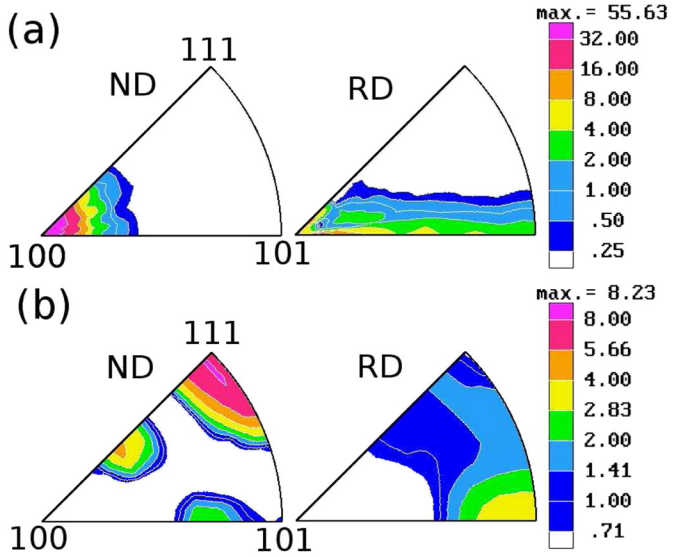

Fig. 8. Inverse pole figures. (a) TRC and (b) SC strip.

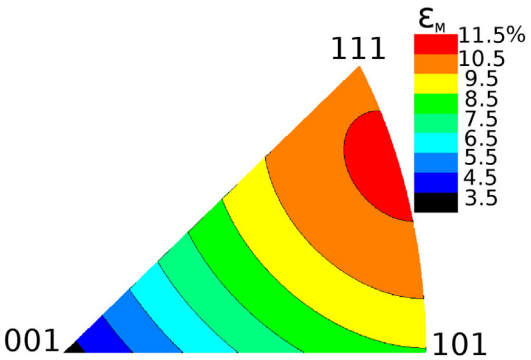

Fig. 9. Maximum transformation strain (ε_M) expressed by contour lines on the *B2* phase reference system. The maximum value (>10%) is reached in the $[355]_{B2}$ direction.

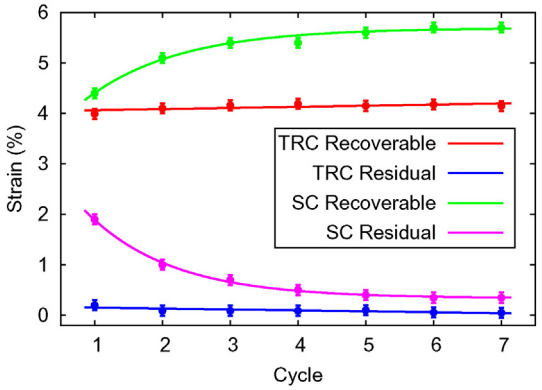

Fig. 11. Recovered and residual strain per cycle as a function of the number of cycles of the TRC and SC strips. Applied load 90 MPa.

that the TRC texture is less favorable than that resulting from the SC process.

3.6. Load-biased thermal cycles

At a constant load of 90 MPa, several thermomechanical cycles were performed on both types of strips (Fig. 10). On one hand, the TRC sample exhibits a high degree of stability of the martensitic transformation. That is the total strain was almost the same over the cycles and the residual strain per cycle was very small and slowly decreased with each successive thermal cycle. On the other hand, the thermomechanical behavior of the SC sample changed markedly during the first five cycles. The residual strain after the first cycle was 1.9%, and it decreased to 0.4% by the fifth cycle. In addition, the transformation hysteresis width remained nearly constant at about 30 K for the TRC strip. However, in the SC strip, the transformation hysteresis grows from 44 K to 50 K with successive thermal cycles.

The recoverable and residual strain measured from the constant load experiment as a function of the number of cycles for the two kinds of specimens are plotted in Fig. 11. From the first cycles, for the SC sample, a marked change in these strains is observed, although they become

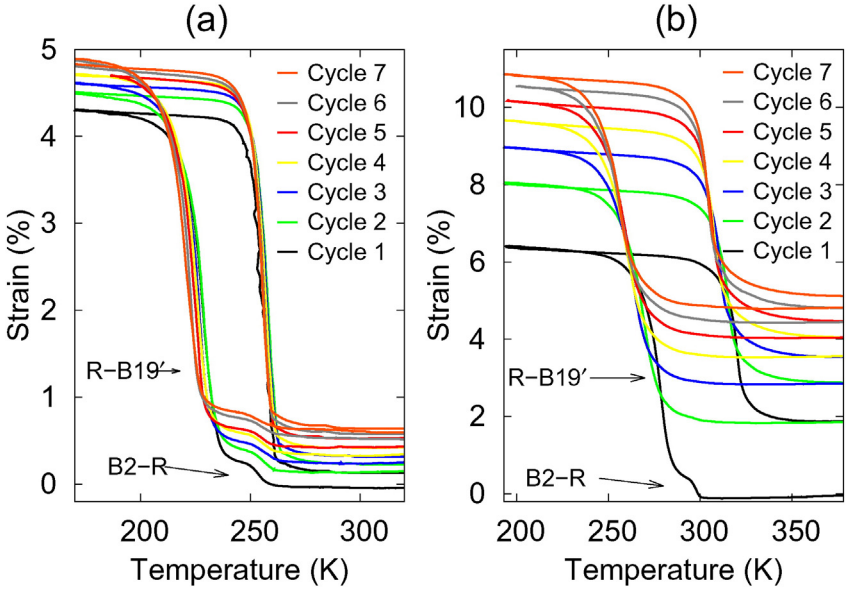

Fig. 10. Strain evolution with temperature during the thermomechanical cycling under constant stress of the (a) TRC and (b) SC strips. Applied load 90 MPa.

almost stable after the fifth cycle. Conversely, in the TRC sample, the recoverable and residual strain remain nearly unchanged from the first cycle. Such load-biased thermal-cycling data evolution reflects the more stable behavior of the strain-temperature curves of the TRC sample (Fig. 10). It is worth noting that the shape memory properties measured here for the TRC strip were obtained on as-cast samples. No heat treatment was applied to the strip in order to improve its properties.

The two-stage transformation observed during cooling in the DSC curves is also manifested in the mechanical behavior. A small curve inflection is clearly observed on the cooling branch of the first loop of both samples, and it can be attributed to the austenite–*R*-phase transformation. The deformation induced by this transformation is very small (lower than 0.4%). This curve inflection is observed in all subsequent cycles of the TRC sample, but disappears after the first cycle in the SC sample. Over the heating path, no significant shape change in the curve related to a two-step transformation could be observed for any sample. This is not surprising if we bear in mind the small differences between A_s and R_s^h, and the fact that the slope of the Clausius-Clapeyron relationship is steeper for the *R*-phase forward transformation than for the martensitic transformation to the B2 structure [46].

In order to measure the maximum recoverable strain, samples TRC as-cast and SC annealed were thermal cycled under different loads. These cycles are shown in Fig. 12, where the response to growing levels of load can be observed. The samples used in this experiment were in the same condition as those cycled under a constant load of 90 MPa. The recoverable strains grow as the load increases up to a value of around 110 MPa for the two types of specimens. At higher load levels, although the maximum value of transformation strain increases, the residual strain magnitude increases similarly, and thus no significant net rise in the recovery strain is observed. However, we must remark on some distinctive aspects of the strain recovery. The residual strains per cycle of the TRC strip are rather small for loads below 90 MPa, and they remain low below 0.6%. In contrast, for the SC samples, the residual strains are already important at low levels of load, and they increase in a roughly proportional manner with the applied external force. It is worth noting that the TRC and SC samples show large recoverable strain and relative low degree of residual strain at a load of 90 MPa. This was the reason for choosing that load to perform the thermal cycle under constant load in Figs. 10 and 11.

The recoverable strains as a function of load are shown in Fig. 13. The recoverable strain of the TRC strip reaches the value of 5.5%, which is quite close to the Sachs' bound value of $5.6 \pm 0.5\%$, calculated in Section 3.5. This close agreement demonstrates the excellent performance of this type of rapid-solidification *Ni–Ti*-based polycrystal. It occurs because of the high compatibility of the martensitic transformation between neighboring columnar grains in a strip with the $\{100\}_{B2}$ solidification texture. Such compatibility arises from intrinsic properties of the $B2 \rightarrow B19'$ martensitic transformation in NiTi alloys. This will be addressed in the next section.

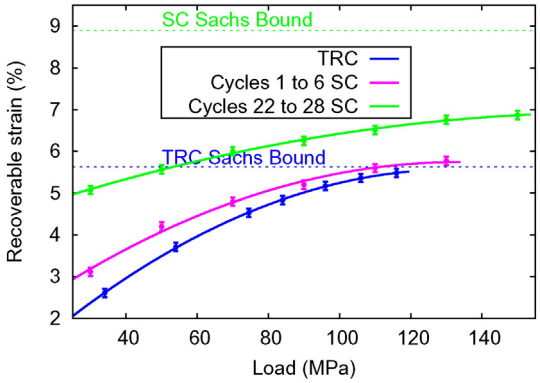

Fig. 13. Recovered strain as a function of load stress during the thermal-cycles.

On the other hand, the SC strip reaches a recoverable strain of 5.8% in the first six cycles, which is slightly higher than the value measured for the TRC strip, but is far from the SC strip Sachs' bound. Nevertheless, following the behavior observed in Fig. 11, an additional increase in the recoverable strain might be expected, if the specimens were cycled further at a given load.

Thus, in the search for treatments to optimize mechanical properties, experiments combining thermal cycling with increases in the applied load and thermal cycling under constant load were performed on SC specimens. Fig. 13 shows the recoverable strain as a function of load from 30 to 150 MPa, after intermediate cycling, cycles 7 to 21 of the sample at 90 MPa. Intermediate cycling at higher loads was not appropriate due to the high residual strains involved. The maximum recoverable strain from these treatments reached a value close to 6.9%. This is a high value of recoverable strain, although it is still 2% below the SC strip Sachs' bound value of 8.9%.

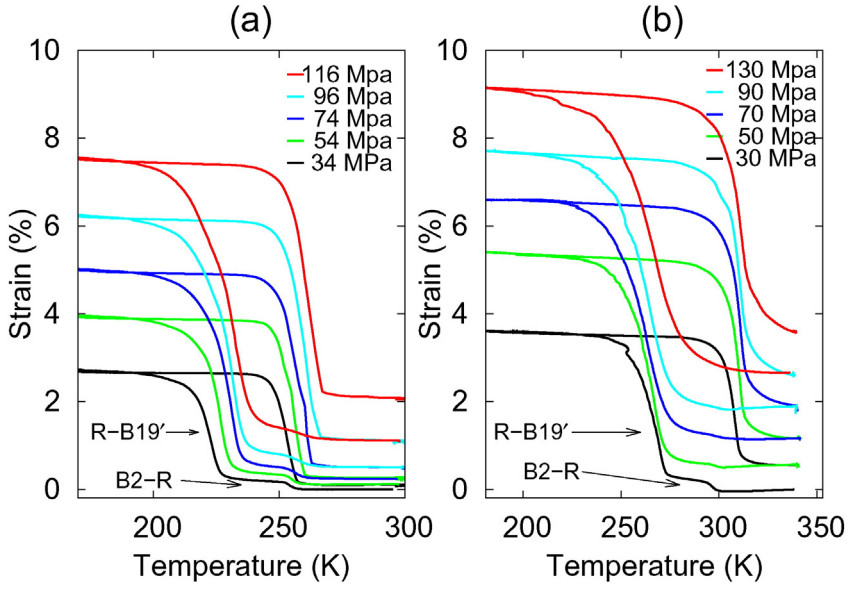

Fig. 12. Strain during the thermal-cycles for different tensile stresses. (a) TRC (b) SC strip.

4. Discussion

The Sachs' bound, or upper bound, provides an interesting tool to examine the effects of TRC and SC microstructures on the strip shape properties.

The loaded, TRC-strip, thermal cycles show that the maximum recoverable strain value is close to the Sachs' bound, and the cycles are completed without leaving behind a significant residual strain. This indicates that the particular TRC microstructure produces minimal constraint between grains, such that in this polycrystalline array almost all the grains transform into a unique martensitic variant when the applied load is high enough. This low degree of grain constraint results from a unique and special concurrence of favorable factors. Firstly, there is an optimal combination of intrinsic features of the martensitic transformation in Ni–Ti alloys (i.e. available transformation variants according symmetry relationships between parent and product phase [47,48,49] and compatibility between transformation strains in different crystal directions and elastic anisotropy [50]). Secondly, the rapid solidification texture permits the grain to take advantage of these unique transformation properties (the reader can see reference [22] for more details on this point).

To the contrary, the SC strip maximum recoverable strain is significantly lower than the corresponding Sachs' bound. This suggests that the strip's microstructure inhibits the transformations in some grains or precludes the appearance of the most favorable variant. That is, the transformation begins in isolated well-oriented grains and saturates due to the formation of a network of fully transformed poorly oriented grains [51]. These transformation constraints are relaxed to some extent when successive cycles are performed, as observed in our experiments, although the maximum recoverable strain remains below the calculated upper bound for the material. Accordingly, Richards et al. [52] studied the interplay between the martensitic phase transformation and plastic slip in a polycrystalline media subject to superelastic cycles. They showed that the plastic deformation (produced by the martensitic transformation) provides a bridge across poorly oriented and non-transforming grains. Besides, the residual stress fields yield a much more disperse transformation over subsequent loadings. In the same way, Yawny et al. [11] asserted that the forward-transformation critical stress decreases as the cycle number increases. They proposed a microstructural scenario to explain this effect. In the first loading, the dislocations are needed to accommodate the martensitic variant needle growth. When the needle goes back on unloading, the dislocations remain in the austenite phase. In the second loading, the stress field created by these dislocations promotes the formation and growth of martensite variants favored by the applied load, decreasing the transformation critical stress.

The effect of the constraint between grains is also observed in the thermal cycles under constant load. The high stability in successive cycles of the TRC strip contrasts with the sharp change in the first cycles of the SC strip (see Fig. 10).

Analysis of the hysteresis also provides indicators of the martensitic transformation performance in a Ni–Ti polycrystal. Gall and Maier [53] and Jaeger et al. [54] showed that samples with small hysteresis width also exhibit lower irreversible strains. As highlighted in Section 3.6, the hysteresis width of the TRC sample is about 20 *K* smaller than the hysteresis of the SC sample. This fact is in concordance with the lower irreversible strain measured in the TRC samples. Such a difference in the hysteresis value corresponds directly to the degree of difficulty for the martensitic transformation in each type of polycrystalline microstructure. Lower compatibility between grains means more obstacles for the transformation, so the increase in hysteresis width can be rationalized based on a higher interface friction and dissipative effects when martensite plates interact with incompatible grain boundaries. Part of this dissipative interaction relaxes in the form of defect generation, mainly dislocations [55], and in an irreversible microplasticity which accumulates and leads to the residual strain left behind when the cycle is completed (Figs. 10 (b) and 11).

5. Summary and conclusion

The present work investigates the effect of the two production techniques, twin-roll casting and standard processing, on the microstructure and corresponding variations in the mechanical properties of Ni_{50-x}–Ti_{50}–Co_x shape memory alloys.

On the one hand, the TRC microstructure yields a very low constraint between grains and high stability of the martensitic transformation. The measured recoverable strain was 5.5%, with a low or negligible residual strain for loads below 90 MPa.

On the other hand, the suitable austenitic texture of the SC strip (the Sachs' bound value is 8.9%) is frustrated by the microstructure, which inhibits the transformations in some grains and precludes the appearance of the most favorable variant. For a load of 90 MPa, the measured maximum recoverable strain was 5.8% in the first cycles, while a residual strain of 1.9% was already introduced in the first cycle. These transformation constraints are partially relaxed after successive cycles are performed, and a maximum recoverable strain of 6.9% is reached while the residual strain decreases to 0.4% at 90 MPa.

The large recoverable deformation without accumulative residual strain, narrow hysteresis, and stability in the load-biased transformation regime at moderate stress levels, make Ni–Ti-based TRC specimens very advantageous for some applications, like actuator devices.

Acknowledgements

The authors would like to thank Daniel Castelani, Javier Cruceño and Pablo Díaz for their valuable collaborations in the development and implementation of the instrumentation used in these experiments. We gratefully acknowledge finantial support from the “Agencia Nacional de Promoción Científica y Tecnológica” (under grants PICT 2140 and PICT 3140) and the argentine-french ECOS program (project A10E02).

References

[1] J.M. Jani, M. Leary, A. Subic, M.A. Gibson, A review of shape memory alloy research, applications and opportunities, Mater. Des. 56 (April 2014) 1078–1113.
[2] H. Hideki, S. Hanada, K. Inoue, T. Fukui, Y. Mishima, T. Suzuki, Martensite transformation temperatures and mechanical properties of ternary NiTi alloys with offstoichiometric compositions, Intermetallics 6 (4) (January 1998) 291–301.
[3] T. Goryczka, Martensitic transformation in NiTiCo strip produced by twin roll casting, Mater. Sci. Eng. A 481-482 (May 2008) 676–679.
[4] A. Ishida, Effects of Grain Size and Co Addition on the Transformation Temperatures of Ti–Ni–Zr Thin Films, Shape Memory and Superelasticity, 2015.
[5] L. Jordan, M. Masse, A. Villafana, G. Bouquet, Effects of Thermal Treatments on the Respective Behaviour of R and Martensitic Phases in Ni–Ti–Co Shape Memory Alloys, Proceedings of the Int. Conf. on Martensitic Tranf. ICOMAT 92 Ed, Monterey Institute for Advanced Studies, USA 1993, pp. 635–640.
[6] Y. Kishi, Z. Yajima, Relation between tensile deformation behavior and microstructure in a tinico shape memory alloy, Mater. Trans. 43 (5) (2002) 834–839.
[7] R.M. Manjeri, D. Norwich, F. Sczerzenie, X. Huang, M. Long, M. Ehrlinspiel, A study of thermo-mechanically processed high stiffness NiTiCo shape memory alloy, J. Mater. Eng. Perform. (2016).
[8] A. Fasching, D. Norwich, T. Geiser, G.W. Paul, An evaluation of a NiTiCo alloy and its suitability for medical device applications, J. Mater. Eng. Perform. 20 (4-5) (2011) 641–645.
[9] R.A. Ahmed, Electrochemical properties of Ni47 Ti49 Co4 shape memory alloy in artificial urine for urological implant, Ind. Eng. Chem. Res. 54 (34) (2015) 8397–8404.
[10] S. Miyazaki, Y.Q. Fu, W.M. Huang (Eds.), Thin Film Shape Memory Alloys, Cambridge University Press, New York, 2009.
[11] A. Yawny, M. Sade, G. Eggeler, Pseudoelsaticity cycling of ultra-fine-grained Ni–Ti shape memory wires, Int. J. Mater. Res. Adv. Tech. 96 (2005) 608.
[12] M. Stian, Ueland and Christopher A Schuh. Superelasticity and fatigue in oligocrystalline shape memory alloy microwires, Acta Mater. 60 (1) (2012) 282–292.
[13] J.-l. Liu, H.-y. Huang, J.-x. Xie, Superelastic anisotropy characteristics of columnar-grained Cu–Al–Mn shape memory alloys and its potential applications, Mater. Des. 85 (2015) 211–220.
[14] D. Sanjeev, N.S. Lim, H.W. Kim, C.G. Park, Effect of rolling speed on microstructure and age-hardening behaviour of Al–Mg–Si alloy produced by twin roll casting process, Mater. Des. 32 (8-9) (2011) 4603–4607.
[15] X. Gong, S.B. Kang, S. Li, J.H. Cho, Enhanced plasticity of twinroll cast ZK60 magnesium alloy through differential speed rolling, Mater. Des. 30 (9) (2009) 3345–3350.
[16] F. Dalle, G. Despert, P. Vermaut, R. Portier, A. Dezellus, P. Plaindoux, P. Ochin, Ni49·8Ti42.2 Hf8 shape memory alloy strips production by the twin roll casting technique, Mater. Sci. Eng. A 346 (2003) 320–327.

[17] S. Eucken, J. Hirsch, E. Hornbogen, Texture and microstructure of meltspun shape memory alloys, Textures and Microstruct. 8 & 9 (C) (1988) 415–426.
[18] B. Kockar, I. Karaman, J.H. Kim, Y.I. Chumlyakov, J. Sharp, C.-J.(.M.). Yu, Thermomechanical cyclic response of an ultrafine-grained NiTi shape memory alloy, Acta Mater. 56 (14) (2008) 3630–3646.
[19] C.E. Sobrero, P. La Roca, a. Roatta, R.E. Bolmaro, J. Malarría, Shape memory properties of highly textured CuAlNi(Ti) alloys, Mater. Sci. Eng. A 536 (February 2012) 207–215.
[20] S.C.C. Mao, J.F.F. Luo, Z. Zhang, M.H.H. Wu, Y. Liu, X.D.D. Han., EBSD studies of the stress-induced B2B19 martensitic transformation in NiTi tubes under uniaxial tension and compression, Acta Mater. 58 (9) (May 2010) 3357–3366.
[21] S. Miyazaki, V.H. No, K. Kitamura, A. Khantachawana, H. Hosoda, Texture of Ti–Ni rolled thin plates and sputter-deposited thin films, Int. J. Plast. 16 (2000) 00004–00008.
[22] L. Isola, P. La Roca, a. Roatta, Philippe Vermaut, L. Jordan, P. Ochin, and J. Malarría. Load-biased martensitic transformation strain of Ti50Ni47Co3 strip obtained by a twin-roll casting technique. Materials Science and Engineering: A, pages 245–252, March.
[23] Y.C.C. Shu, K. Bhattacharya, The influence of texture on the shape-memory effect in polycrystals, Acta Mater. 46 (15) (September 1998) 5457–5473.
[24] J.A. Monroe, I. Karaman, D.C. Lagoudas, G. Bigelow, R.D. Noebe, S. Padula, Determining recoverable and irrecoverable contributions to accumulated strain in a NiTiPd high-temperature shape memory alloy during thermomechanical cycling, Scr. Mater. 65 (2) (July 2011) 123–126.
[25] N.G. Jones, D. Dye, Martensite evolution in a NiTi shape memory alloy when thermal cycling under an applied load, Intermetallics 19 (10) (October 2011) 1348–1358.
[26] K.C. Atli, B.E. Franco, I. Karaman, D. Gaydosh, R.D. Noebe, Influence of crystallographic compatibility on residual strain of TiNi based shape memory alloys during thermo-mechanical cycling, Mater. Sci. Eng. A (March 2013).
[27] S. Padula, S. Qiu, D. Gaydosh, R. Noebe, G. Bigelow, A. Garg, R. Vaidyanathan, M. Society, Effect of upper-cycle temperature on the load-biased, strain-temperature response of NiTi, Metall. Mater. Trans. A 43 (12) (June 2012) 4610–4621.
[28] T. Goryczka, P. Ochin, Characterization of a Ni50Ti50 shape memory strip produced by twin roll casting technique, J. Mater. Process. Technol. 162-163 (May 2005) 178–183.
[29] C. Sobrero D. Castellani, R. Bolmaro, and J. Malarría. Stage for texture measurements above room temperature in a Philips X'Pert Pro MPD diffractometer. The Review of scientific instruments, (11):113903, November.
[30] J.S. Kallend, U.F. Kocks, A.D. Rollett, H.R. Wenk, Operational texture analysis, Mater. Sci. Eng. A 132 (1991) 1–11.
[31] L. Lutterotti, Maud (Material Analysis Using Diffraction), April 2015.
[32] D.L. Kaiser, J.R.L. Watters, Standard Reference Material ®660b, 2010.
[33] T. Hahn (Ed.), International Tables for Crystallography Volume A: Space-group symmetry, fifth ed.Springer, Netherlands, 2002.
[34] J. Khalil-Allafi, W.W. Schmahl, M. Wagner, H. Sitepu, D.M. Toebbens, G. Eggeler, The influence of temperature on lattice parameters of coexisting phases in NiTi shape memory alloys - a neutron diffraction study, Mater. Sci. Eng. A 378 (1-2) (July 2004) 161–164.
[35] H. Sitepu, W.W. Schmahl, J.K. Allafi, G. Eggeler, A. Dlouhy, D.M. Toebbens, M. Tovar, Neutron diffraction phase analysis during thermal cycling of a Ni-rich NiTi shape memory alloy using the Rietveld method, Scr. Mater. 46 (2002) 543–548.
[36] J. Olbricht, A. Yawny, J.L. Pelegrina, A. Dlouhy, G. Eggeler, Materials Society, On the stress-induced formation of R-phase in ultra-fine-grained Ni-rich NiTi shape memory alloys, Metall. Mater. Trans. A 42 (9) (April 2011) 2556–2574.
[37] P. Olier, F. Barcelo, J.L. Bechade, J.C. Brachet, E. Lefevre, G. Guenin, Effects of impurities content (oxygen, carbon, nitrogen) on microstructure and phase transformation temperatures of near equiatomic TiNi shape memory alloys, J. Phys. IV France 07 (1997) (1997) (C5–143–C5–148).
[38] V. Ph, M. Lamicol, M. Hytch, P. Ochin, R. Portier, Multiple martensitic transformation induced by coherent precipitation in NiTiCo melt spun ribbons, J. Phys. IV France 11 (2001) 451–456.
[39] T. Simon, A Kröger, C. Somsen, A. Dlouhy, G. Eggeler, On the multiplication of dislocations during martensitic transformations in NiTi shape memory alloys, Acta Mater. 58 (2010) 1850–1860.
[40] W. Tang, R. Sandström, Analysis of the influence of cycling on TiNi shape memory alloy properties, Mater. Des. 14 (2) (1993) 103–113.
[41] R. Santamarta, E. Cesari, J. Pons, T. Goryczka, Shape memory properties of Ni–Ti based melt-spun ribbons, Metall. Mater. Trans. A 35 (March) (2004) 761–770.
[42] T. Goryczka, Structure and shape memory effect in annealed Ni–Ti–Co strip produced by twin roll casting technique, Solid State Phenom. 154 (April 2009) 59–64.
[43] J. Khalil-Allafi, B. Amin-Ahmadi, The effect of chemical composition on enthalpy and entropy changes of martensitic transformations in binary NiTi shape memory alloys, J. Alloys Compd. 487 (2009) 363–366.
[44] G. Laplanche, a. Kazuch, G. Eggeler, Processing of NiTi shape memory sheets microstructural heterogeneity and evolution of texture, J. Alloys Compd. 651 (2015) 333–339.
[45] P. Šittner, V. Novák, Anisotropy of martensitic transformations in modeling of shape memory alloy polycrystals, Int. J. Plast. 16 (2000) 1243–1268.
[46] J. Kim, S. Miyazaki, Effect of nano-scaled precipitates on shape memory behavior of Ti-50.9at.%Ni alloy, Acta Mater. 53 (17) (October 2005) 4545–4554.
[47] K. Bhattacharya, R.V. Kohn, Symmetry, texture and the recoverable strain of shapememory polycrystals, Acta Mater. 44 (2) (February 1996) 529–542.
[48] K. Bhattacharya, S. Conti, G. Zanzotto, J. Zimmer, Crystal symmetry and the reversibility of martensitic transformations, Nature 428 (March) (2004) 55–59.
[49] K. Otsuka, A. Saxena, J. Deng, X. Ren, Mechanism of the shape memory effect in martensitic alloys: an assessment, Philos. Mag. 91 (December 2011) (2011) 4514–4535.
[50] P. Šittner, Y. Liu, V. Novák, On the origin of Lüders-like deformation of NiTi shape memory alloys, J. Mech. Phys. Solids 53 (8) (August 2005) 1719–1746.
[51] K. Bhattacharya, A. Schl¨omerkemper, Stress-induced phase transformations in shape-memory polycrystals, Arch. Ration. Mech. Anal. 196 (2010) 715–751.
[52] A.W. Richards, R.A. Lebensohn, K. Bhattacharya, Interplay of martensitic phase transformation and plastic slip in polycrystals, Acta Mater. 61 (12) (2013) 4384–4397.
[53] K. Gall, H.J. Maier, Cyclic deformation mechanisms in precipitated NiTi shape memory alloys, Acta Mater. 50 (2002) 4643–4657.
[54] S. Jaeger, B. Maaß, J. Frenzel, M. Schmidt, J. Ullrich, S. Seelecke, A. Schütze, O. Kastner, G. Eggeler, On the widths of the hysteresis of mechanically and thermally induced martensitic transformations in NiTi-based shape memory alloys, Int. J. Mater. Res. 106 (2015) 1029–1039.
[55] A.M. Condó, F.C. Lovey, J. Olbricht, C. Somsen, A. Yawny, Microstructural aspects related to pseudoelastic cycling in ultra fine grained NiTi, Mater. Sci. Eng. A 481-482 (May 2008) 138–141.